

Performance Evaluation of Vectorized NavIC Receiver Using Improved Dual-Frequency NavIC Measurements

Abhijit Dey¹, Member, IEEE, Kaushik Iyer², Bing Xu³, Member, IEEE,
Nitin Sharma⁴, and Li-Ta Hsu⁵, Senior Member, IEEE

Abstract—This article presents a modified carrier-aided dual-frequency vectorized tracking (CA-DFVT) algorithm for Navigation with Indian Constellation (NavIC) receiver. In signal blockage and interference scenarios, even the most advanced receiver architecture may fail to provide accurate positioning solutions. Therefore, this article proposes an improved CA-DFVT architecture for NavIC signals. The architecture is based on the vector delay frequency lock loop (VDFLL), wherein precise carrier phase measurements from NavIC *S* and unambiguous code phase measurements from the *L5* signal are integrated to form new measurements. These measurements are improved by the novel vector tracking (VT) approach introduced in this article. The approach adopts the Savitzky–Golay filtering technique to improve the integrated measurements without deforming the actual measurements. Furthermore, the improved CA-DFVT receiver architecture includes a bidirectional algorithm called the Rauch–Tung–Striebel (RTS). This process involves a forward estimation extended Kalman filter (EKF) and a backward recursion smoother. In addition, this article also introduces VT for CA-DFVT based on an unscented Kalman filter (UKF). Simulations and hardware implementation are carried out to evaluate the effectiveness of the proposed algorithm under conditions of signal blockage and interference. Experiments demonstrate that the improved CA-DFVT can achieve better position accuracy than the single-frequency *L5/S* VT, CA-DFVT-EKF, and CA-DFVT-UKF approaches. The mean position accuracy of improved CA-DFVT improves by at least 2–6 and 1–2 m for signal blockage and interference conditions, respectively.

Index Terms—Extended Kalman filter (EKF), Navigation with Indian Constellation (NavIC), Rauch–Tung–Striebel (RTS), Savitzky–Golay filter, software-defined receiver, unscented Kalman filter (UKF), vector tracking (VT).

Manuscript received 29 October 2022; revised 4 June 2023; accepted 24 June 2023. Date of publication 13 July 2023; date of current version 26 July 2023. This work was supported in part by the Science and Engineering Research Board (SERB) Project under Grant CRG/2021/006784 and in part by the Guangdong Basic and Applied Basic Research Foundation Project under Grant 2022A1515011680. The Associate Editor coordinating the review process was Dr. Martti Kirkko-Jaakkola. (Corresponding author: Abhijit Dey.)

Abhijit Dey and Nitin Sharma are with the Department of Electrical and Electronics Engineering, Birla Institute of Technology and Science Pilani, K K Birla Goa Campus, Sancoale, Goa 403726, India (e-mail: abhijitdey89@gmail.com; nitinn@goa.bits-pilani.ac.in).

Kaushik Iyer is with the Department of Electrical Engineering, Arizona State University, Tempe, AZ 85281 USA (e-mail: kiyer2396@gmail.com).

Bing Xu and Li-Ta Hsu are with the Department of Aeronautical and Aviation Engineering, The Hong Kong Polytechnic University, Hong Kong SAR, China (e-mail: pbing.xu@polyu.edu.hk; lt.hsu@polyu.edu.hk).

Digital Object Identifier 10.1109/TIM.2023.3295020

I. INTRODUCTION

THE recent development of an Indian satellite system called Navigation with Indian Constellation (NavIC) has emerged and become a ubiquitous system. It provides highly accurate positioning and timing information in India and its near boundaries [1]. However, the positioning accuracy and reliability of navigation solutions using NavIC receiver depend significantly on the availability and quality of received signals [2]. Vehicle and/or pedestrian positioning using the NavIC system in urban environments faces two significant problems: signal attenuation and interference from unlicensed *S*-band sources [3]. Therefore, obtaining better position accuracy for pedestrians and/or vehicles moving on downtown streets is highly challenging. The unlicensed industrial, scientific, and medical radio band (ISM)-bands, such as 2.4-GHz *S*-band signals, are widely used in different applications. For instance, wireless fidelity (Wi-Fi), Bluetooth, worldwide interoperability for microwave access (WiMax), and long-term evolution (LTE) are the most common systems that work on *S*-band signals. These signals act as an unintentional out-of-band interference for NavIC *S*-band (2492.028 MHz), resulting in decreased positioning accuracy. In addition, the pulsed signals from aeronautic radio-navigation services (ARNSSs), such as tactical air navigation (TACAN), multifunction information distribution system (MIDS), distance measuring equipment (DME), and joint tactical information distribution system (JTIDS), act as an unintentional in-band interference for NavIC *L5*-band (1176.45 MHz) [4]. Thus, the dependence of several safety- and liability-critical applications on NavIC necessitates the improvement of its robustness against various signal vulnerabilities.

Since NavIC uses spread-spectrum technology, it has anti-jamming capabilities, making it resistant to intentional or unintentional interference to some extent. However, if the interference power exceeds the processing gain of NavIC, the receiver performance degrades, even to the point of complete failure. Furthermore, NavIC receivers with traditional federated architecture can hardly track dynamic weak signals, as it tracks each satellite independently using an individual signal processing unit and a common navigation processing unit driven by the pseudoranges. Each signal processing unit performs code and carrier frequency/phase tracking using

delay-locked loops (DLLs) and frequency-locked loop (FLL) or phase-locked loop (PLL).

Both Doppler frequencies and pseudoranges exhibit substantial correlation with the clock bias of the receiver and the motion of the satellite/receiver. This element, however, is overlooked in federated receiver architectures. One possible solution is to deeply integrate the signal processing and navigation processors, in which the navigation processor controls both the code and the carrier numerically controlled oscillators (NCOs), also known as vector tracking (VT) (or VT loops) [5]. In vectorized receivers, the tracking of satellites is achieved using the Kalman navigation filter. The navigation filter combinedly performs the task of tracking and calculation of navigation solution integrated in one algorithm [6]. This improves the performance of the signal processing of the global navigation satellite system (GNSS) instrument in challenging environments with the support of the position and velocity solutions.

Existing literature [7], [8], [9], [10] presented the review of different state-of-the-art receiver architecture based on VT that focused on analyzing the performance of VT loops over conventional scalar tracking loops (federated receivers) to highlight its benefits. Here, we generalize the performance analyses into two main categories.

The first category of performance analyses involves studying the efficacy of single-frequency VT receiver architecture in signal challenging environments. For instance, Lashley et al. [11] analyzed the performance of VT algorithm for weak global positioning system (GPS) signals under high dynamics. Lashley et al. [11] performed an extensive analysis based on different carrier-to-noise ratios (C/N_0) to demonstrate the ability of VT to track weak signals. Xu et al. [12] modified the vector delay lock loop (VDLL)-based VT algorithm to detect and correct the GNSS non-line-of-sight (NLOS) signals. Pany and Eissfeller [13] presented a case study of the VDLL under insufficient signal strength, which includes indoor signal reception and signal outage. Pany and Eissfeller [13] qualitatively used the discriminator outputs to show the continuity of tracking under harsh environments without going into a reacquisition mode. In addition, the work in [14] performed a more generalized study on the performance of VT, emphasizing on comparison of positioning results between a federated receiver and vectorized receiver when fewer satellites were available.

Another category involves the performance assessment of multifrequency and/or multiconstellation GNSS VT receiver architectures. For instance, Tabatabaei et al. [15] presented an integrated GPS and GLONASS vectorized receiver and performed its performance assessment in [16]. In [16], the analysis was limited to satellite availability and trajectory estimation based on the increase in the number of satellites due to the multi-GNSS approach. A similar approach was reported in [17], where an integrated GPS and Galileo VT algorithm was presented. Shytermeja et al. [17] used ionospheric delays estimation as extended Kalman filter (EKF) states and tested the performance for the scenarios with multipath and ionospheric scintillations.

The main feature of VT receiver architecture lies in the performance of the EKF, as it integrates the tracking and navigation algorithms. Hence, it is important to evaluate these architectures based on its EKF parameters. In this context, Chen et al. [18] presented the performance evaluation of an adaptive iterative EKF, where statistical figures of merit were used to quantify its performance. Similarly, different types of Kalman filter algorithms for VT in deep integration/ultratight coupling were compared in [19]. In [19], the comparison was based on the effective carrier phase estimation. In addition, the work in [20] compares the performance of EKF sigma point Kalman filters based on filter parameters and positioning results. An EKF-based analysis for a GPS signal tracking loop was reported by Tang et al. [21], where they presented qualitative and quantitative results on the stability and convergence of the EKF.

In an effort to cast insight into the problem of interference in NavIC *S*-band and *L5*-band signals, and methodologies for improvement of receiver robustness in high dynamics, Dey et al. [22] presented a carrier-aided dual-frequency vectorized tracking (CA-DFVT) architecture for NavIC signals. It recasts a novel carrier-aided approach where the precise carrier phase measurements of one frequency and unambiguous code phase measurements from another frequency were combined to form improved measurements. In CA-DFVT, measurements of the carrier phase from NavIC *S* signal and pseudorange measurements from NavIC *L5* are combined to generate better measurements provided as input to the EKF. This improves the estimates of position, velocity, and time (PVT) at the output of EKF. With the help of the developed dual-frequency receiver architecture and experimental results, Dey et al. [22] established that the performance of a single-frequency NavIC vectorized receiver can be enhanced by aiding carrier phase measurements in a dual-frequency approach.

The work presented in [22] was limited to evaluating the performance of CA-DFVT in static and dynamic environments. However, scenarios, such as signal attenuation and interference, were not considered. In fact, due to urbanization, most GNSS receivers experience severe signal interference or attenuation from high-rise buildings and interference from terrestrial equipment. As a result, even the advanced receiver struggles to perform well in such vulnerabilities, resulting in signal outages or degradation in navigation solutions. Despite the fact that the measurement model was a novel approach in [22], EKF stability and measurement residue analysis were not carried out. A residue analysis is imperative to ensure that the receiver tracking architecture retains a stable region of operation in a signal-constrained environment.

In addition, traditional VT approaches mainly employed EKF as their main position estimator. In EKF, the nonlinear system model is linearized by the first-order Taylor expansion such that the traditional Kalman filter can be applied. Despite its widespread adaptation in GNSS, the large estimation error due to the linearization of the system model motivated researchers to investigate alternative filters, such as the unscented Kalman filter (UKF) [23], [24], for improving

the accuracy of positioning solutions during GNSS signal vulnerabilities. To the best of our knowledge, there has been no research on multifrequency VT employing UKF as a position estimator.

This article proposes an improved version of the CA-DFVT receiver architecture. The modification in the proposed VT approach includes a bidirectional filtering algorithm called Rauch–Tung–Striebel (RTS) smoother and measurement smoothing using the Savitzky–Golay filter. More emphasis is given to the EKF analysis and positioning results obtained through different field experiments conducted in signal blockage and interference conditions. New testbeds are developed, and a description of the process for measuring NavIC signals under these conditions is provided. The residue error analysis and trend of each state vector element of the improved measurement model are carried out in the EKF analysis. In addition, for comparison, a UKF-based estimator is also presented in this article for CA-DFVT. The main contributions of this article are given as follows.

- 1) The integrated measurements of CA-DFVT are further improved by using the Savitzky–Golay filter to filter the additional noise terms without deforming the actual measurements.
- 2) For position estimation, a novel bidirectional vectorized tracking approach that involves a forward estimation and a backward recursive smoothing process is presented. The forward estimation is achieved by EKF, while the backward filtering is achieved by the RTS backward recursion smoother.
- 3) A UKF-based estimation approach for the CA-DFVT receiver architecture is presented. A detailed description of the implementation procedure of UKF for VT is discussed, and its results are compared with single-frequency $L5/S$, CA-DFVT-EKF, and the proposed improved version of CA-DFVT.
- 4) Additional instruments were deployed for generating Wi-Fi and Bluetooth interference and acquiring the NavIC and interference measurements using the radio frequency (RF) front end. For the signal blockage/attenuation dynamic test scenario, the measurement setup was developed and deployed in a car for signal collection. A car equipped with the instrumental setup was driven through a blockage area, where satellite visibility was temporarily blocked.
- 5) An extensive PVT estimation performance analysis based on real-data measurements collected in interference and signal blockage/attenuation scenarios is presented. The Wi-Fi and Bluetooth interference test demonstrates the robustness of the receiver architecture under interference from Wi-Fi, Bluetooth, and LTE signals, whereas the signal blockage/attenuation test is particularly presented to demonstrate the superior performance of improved CA-DFVT compared to conventional single-frequency VT, CA-DFVT-EKF, and CA-DFVT-UKF. Moreover, the investigation of C/N_0 values and in-phase (I) and quadrature-phase (Q) prompt correlations based on the collected measurements are presented for both test scenarios.

- 6) Finally, a proper EKF analysis is presented, which includes the analysis of residue errors and the trend of the state vector elements over time. It has been shown that the state vector elements remain within the σ -bounds for the new measurement model in improved CA-DFVT.

These contributions are important as they improve the understanding of the novel improved CA-DFVT receiver architecture by performing EKF- and performance-based analysis under signal challenging situations such as interference and urban canyon positioning. As this is a new approach, the analysis presented in this work will help understand the efficacy of the improved CA-DFVT algorithm and encourage researchers to adopt this for other GNSS systems. In addition, this article highlights the usage of UKF-based navigation filter for multifrequency VT approaches.

The rest of this article is organized as follows. Section II describes the overview of CA-DFVT algorithm, measurement model of improved CA-DFVT using Savitzky–Golay filter, RTS filtering methodology, and UKF formulation. In Section III, the developed receiver is tested in two signal challenging situations, and its detailed performance assessment is presented in Section IV. Finally, Section V concludes this article.

II. IMPROVED CA-DFVT RECEIVER ARCHITECTURE SOFTWARE IMPLEMENTATION

This section revisits the receiver architecture and measurement model of the EKF adopted in the VT loop of CA-DFVT [22]. Section II-A presents the overview of CA-DFVT. Section II-B presents the proposed measurement model of improved CA-DFVT, followed by RTS filtering methodology in Section II-C. The UKF-based receiver methodology is described in Section II-D.

A. Overview of CA-DFVT

In CA-DFVT receiver architecture, the acquisition of satellites is done separately for NavIC S -band and $L5$ signals. The acquired satellites are then tracked using the conventional scalar tracking loops and the ephemerides are decoded. Thereafter, the PVT is computed, and based on the decoded ephemerides and average value of obtained PVT from S -band and $L5$, the VT loop of the CA-DFVT is initialized. At this stage, the tracking of S -band and $L5$ signals are done in an integrated manner. It implements the noncoherent vector delay frequency lock loop (VDPLL), where the novel measurement model utilizes accurate carrier measurements of S -band signals and aids the unambiguous code measurements of $L5$. The code phase $\Delta\tau(t)$ (meters) and the carrier frequency $\Delta f(t)$ (meters/second) residuals obtained from the carrier and code discriminators are applied as input to the EKF for updating the measurements at every epoch k . It is to be noted that both $\Delta\tau(t)$ and $\Delta f(t)$ residuals of $L5$ and only $\Delta f(t)$ residuals of S -band are used as measurements. $\Delta\tau$ and Δf obtained at the discriminator output in the k th epoch corresponding to j th satellite are linked to the position and velocity of the receiver

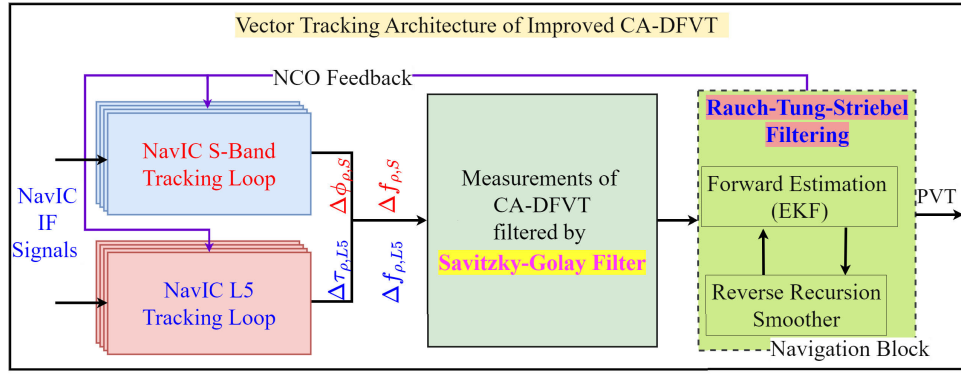


Fig. 1. Block representation of tracking architecture of the improved CA-DFVT.

and can be expressed as

$$\begin{cases} \Delta\tau_{\rho,k}^j = \delta b_k + (\delta\mathbf{p}_k^T)\alpha_k^j + \eta_{\text{code}}^j \\ \Delta f_{\rho,k}^j = \delta\dot{b}_k + (\delta\mathbf{v}_k^T)\alpha_k^j + \eta_{\text{carr}}^j \end{cases} \quad (1)$$

where b is the receiver clock bias in meters and \dot{b} is the drift in meter/second. The estimates of the receiver position and receiver velocity are defined as $\mathbf{p} = [x, y, z]^T$ m and $\mathbf{v} = [\dot{x}, \dot{y}, \dot{z}]^T$ m/s. The superscript T denotes the transpose operator. α^j is the line-of-sight (LOS) unit column vector for the j th satellite and η is the discriminator noise. These $\Delta\tau_k^j$ and Δf_k^j in (1) are used to update the NCO to obtain the true receiver position and velocity at the k th epoch [7], [25].

The instantaneous values of carrier phase $\Delta\phi(t)$ are computed using carrier discriminator measurements, in which $\Delta\phi(t)$ in radians is obtained by integrating the instantaneous Doppler frequency measurements over one measurement epoch. The pseudorange errors at the code discriminator output and pseudorange errors using the carrier phase measurements in units of meters are expressed as

$$\Delta\tau_{\rho}(t) \cdot \lambda = \delta\rho_I(t) + \delta I(t) + \delta\text{Tr}(t) + \eta \quad (2)$$

$$\Delta\phi_{\rho}(t) = \delta\rho_I(t) + \lambda \cdot \delta N + \eta_{\phi}. \quad (3)$$

Fig. 1 shows the VT architecture of the proposed improved version of CA-DFVT for NavIC signals. A detailed explanation of individual blocks of this architecture is provided in Sections II-B and II-C.

B. Measurement Model

As mentioned earlier, the measurement model is formulated as a linear combination of the pseudorange and pseudorange rate residues of the $L5$ - and S -bands. We intend to combine the inherent benefits of the high-frequency S -band, which is less prone to ionospheric delays and has lower noise in the carrier phase with the better noise mitigation capabilities of the $L5$ signal. Moreover, using signals at two distinct frequencies transmitted from the same satellite leads to cancellation of additional error terms in the new pseudorange estimation. The new measurement is formed by taking average of (2) and (3).

The measurement equation for the new pseudorange can be expressed as [22]

$$\begin{aligned} z_{\tau}^j &= \frac{1}{2} [\Delta\tau_{\rho}^j(t) + \Delta\phi_{\rho}^j(t)] \\ &= \frac{1}{2} [\Delta\tau^j(t) \cdot \lambda_{L5} + \Delta\phi^j(t) \cdot \lambda_S] \end{aligned} \quad (4)$$

where z_{τ}^j is the pseudorange error measurement of the j th satellite and λ_S and λ_{L5} denote the wavelengths of NavIC signal in S -band and $L5$ signal, respectively.

Doppler estimates from the carrier discriminator output are used to generate the pseudorange rate measurements. The average value of Δf from both S -band and $L5$ are considered as the accurate measurement, which is given as [22]

$$\begin{aligned} z_f^j &= \frac{1}{2} [\Delta f_{\rho,L5}^j(t) + \Delta f_{\rho,S}^j(t)] \\ &= \frac{1}{2} [\Delta f^j(t) \cdot \lambda_{L5} + \Delta f^j(t) \cdot \lambda_S] \end{aligned} \quad (5)$$

where Δf^j in cycles/second is measured by the carrier discriminator for the j th satellite and is expressed as Δf_{ρ}^j in meter/second. Combining (4) and (5), the EKF measurement vector for M satellites can be expressed as

$$\mathbf{z} = [z_{\tau}^1, z_{\tau}^2, \dots, z_{\tau}^M | z_f^1, z_f^2, \dots, z_f^M]_{2M \times 1}^T. \quad (6)$$

Savitzky and Golay [26] applied on the combined measurements expressed in (6) with the aim of filtering noise terms without deforming the measurements. Since the tracking is done at every 1 ms, subsets of 999 samples are fit using a low-order polynomial with linear least-squares method. Thereafter, the convolution of all the polynomials is obtained. The basic idea of Savitzky–Golay filter is to approximate the underlying signal piece-by-piece locally within a sliding window using polynomial fitting with fixed order [26] with a least-squares estimation algorithm. Mathematically, the Savitzky–Golay filter can be expressed as

$$M_l^* = \frac{\sum_{i=-p}^{i=p} \omega_i M_{l+1}}{N} \quad (7)$$

where M is the original estimated measurements, M^* is the smoothed measurement, ω_i is the coefficient for the i th smoothing, and N is the number of convoluting samples

(i.e., tracking at 1 ms) in the smoothing window size $(2p + 1)$. The index l represents the running index in the filtering process. The smoothing output array consists of $2p + 1$ points, where p is the half-width of the filter window. In the proposed receiver architecture, the window/frame size is selected as 999, whereas the best fit value of polynomial order is selected using a trial-and-error method. In general, an extremely lower order would cause the measurements to lose their meaning, while a very high order would fail to remove the outlier. Therefore, in our case, the order of the polynomial is set to 5.

C. RTS Filtering Methodology

In improved CA-DFVT, the state vector $\delta \mathbf{x}$ is given as

$$\begin{aligned} \delta \mathbf{x} &= [\delta x \quad \delta y \quad \delta z \quad \delta \dot{x} \quad \delta \dot{y} \quad \delta \dot{z} \quad b \quad \delta \dot{b}]^T \\ &= [\delta \mathbf{p}^T \quad \delta \mathbf{v}^T \quad b \quad \delta \dot{b}]_{8 \times 1}^T. \end{aligned} \quad (8)$$

The vectorized tracking of improved CA-DFVT involves a forward estimation and backward recursive smoothing process. The forward estimation is achieved by EKF, while the backward filtering is achieved by RTS backward recursion smoother [27], [28].

1) *Forward Estimation*: The error state covariance matrices \mathbf{P}_0^- and $\delta \mathbf{x}_0^-$ are initialized as follows:

$$\begin{cases} \mathbf{P}_0^- = \text{diag}[10 & 10 & 10 & 1 & 1 & 1 & 1 & 1] \\ \delta \mathbf{x}_0^- = [0 & 0 & 0 & 0 & 0 & 0 & 0 & 0]^T. \end{cases} \quad (9)$$

With this initialization, assuming that $\delta \hat{\mathbf{x}}_k^+$ and \mathbf{P}_k^+ are known, the EKF equations for prediction and measurement update can be expressed as

$$\begin{aligned} \delta \hat{\mathbf{x}}_{k+1}^- &= \Phi \cdot \delta \hat{\mathbf{x}}_k^+ \\ \mathbf{P}_{k+1}^- &= \Phi \mathbf{P}_k^+ \Phi^T + \mathbf{Q} \\ \mathbf{K}_{k+1} &= \mathbf{P}_{k+1}^- \mathbf{H}^T (\mathbf{H} \mathbf{P}_{k+1}^- \mathbf{H}^T + \mathbf{R})^{-1} \\ \delta \hat{\mathbf{x}}_{k+1}^+ &= \delta \hat{\mathbf{x}}_{k+1}^- + \mathbf{K}_{k+1} (\mathbf{z}_{k+1} - \mathbf{H} \cdot \delta \hat{\mathbf{x}}_{k+1}^-) \\ \mathbf{P}_{k+1}^+ &= (\mathbf{I} - \mathbf{K}_{k+1} \mathbf{H}) \mathbf{P}_{k+1}^- \end{aligned} \quad (10)$$

where “+” denotes posterior (updated), “-” denotes prior (predicted) estimate, and \mathbf{K} is the Kalman gain. In (10), Φ is the state transition matrix, which is defined as [22]

$$\Phi = \begin{bmatrix} 0 & 0 & 0 & \Delta t_k & 0 & 0 & 0 & 0 \\ 0 & 0 & 0 & 0 & \Delta t_k & 0 & 0 & 0 \\ 0 & 0 & 0 & 0 & 0 & \Delta t_k & 0 & 0 \\ 0 & 0 & 0 & 0 & 0 & 0 & 0 & 0 \\ 0 & 0 & 0 & 0 & 0 & 0 & 0 & 0 \\ 0 & 0 & 0 & 0 & 0 & 0 & 0 & 0 \\ 0 & 0 & 0 & 0 & 0 & 0 & 1 & \Delta t_k \\ 0 & 0 & 0 & 0 & 0 & 0 & 0 & 0 \end{bmatrix}_{8 \times 8}. \quad (11)$$

\mathbf{H} is the observation matrix, which relates the measurements to $\delta \mathbf{x}$ and is given as [22]

$$\mathbf{H} = \begin{bmatrix} a_x^1 & a_y^1 & a_z^1 & 0 & 0 & 0 & 1 & 0 \\ \vdots & \vdots \\ a_x^M & a_y^M & a_z^M & 0 & 0 & 0 & 1 & 0 \\ 0 & 0 & 0 & a_x^1 & a_y^1 & a_z^1 & 0 & 1 \\ \vdots & \vdots \\ 0 & 0 & 0 & a_x^M & a_y^M & a_z^M & 0 & 1 \end{bmatrix}_{2M \times 8}. \quad (12)$$

\mathbf{Q} and \mathbf{R} are the process and measurement noise covariance matrices, respectively, and \mathbf{Q} and \mathbf{R} are initialized as follows:

$$\mathbf{Q} = \text{diag}[20 \quad 20 \quad 20 \quad 4 \quad 4 \quad 4 \quad 0.01 \quad 0.1] \quad (13)$$

$$\mathbf{R} = \left[\begin{array}{c|c} 800 \times I_M & \mathbf{0} \\ \hline \mathbf{0} & 500 \times I_M \end{array} \right] \quad (14)$$

where I_M denotes an identity matrix of dimension M .

2) *Backward Recursion Smoother*: The backward recursion filtering is applied on $\delta \mathbf{x}^+$ and \mathbf{P}_{k+1}^+ . The smoothing equations can be expressed as [27]

$$\begin{aligned} \mathbf{K}_{k,\text{smooth}} &= \mathbf{P}_k^+ \Phi^T (\mathbf{P}_{k+1}^-)^{-1} \\ \delta \hat{\mathbf{x}}_{k,\text{smooth}} &= \delta \hat{\mathbf{x}}_k^- + \mathbf{K}_{k,\text{smooth}} (\delta \hat{\mathbf{x}}_{k+1,\text{smooth}} - \delta \hat{\mathbf{x}}_{k+1}^-) \\ \mathbf{P}_{k,\text{smooth}} &= \mathbf{P}_k^+ + \mathbf{K}_{k,\text{smooth}} (\mathbf{P}_{k+1,\text{smooth}} - \mathbf{P}_{k+1}^-) \mathbf{K}_{k,\text{smooth}}^T \end{aligned} \quad (15)$$

In this, the loop runs in a backward manner, i.e., if k denotes the current epoch and $k+1$ denotes the previous value. Through this bidirectional filtering method in the improved CA-DFVT, we are able to effectively reduce the variance in the error, resulting in smoother position estimations. Since the RTS backward estimation has its loop running in a backward manner, it is convenient to run the forward and backward processes simultaneously, without causing the computation to increase significantly.

D. Unscented Kalman Filter

The UKF is an unbiased, minimum-mean squared error estimator of a dynamic system [29], [30]. In general, it is an improved version of Kalman filter for nonlinear systems with a similar structure to the EKF. However, unlike EKF, both states and measurements undergo a weighted transformation through symmetrically distributed sigma points. The implementation of UKF for position estimation in CA-DFVT can be done in the following steps [31].

1) *Calculation of Weights (W)*:

$$\begin{aligned} \mathbf{W}_0 &= \frac{\kappa}{n + \kappa} \\ \mathbf{W}_i &= \frac{1}{2(n + \kappa)}; \quad i = 1, 2, \dots, 2n \end{aligned} \quad (16)$$

where κ is a parameter to be tuned ($\kappa = 2$), $n = \dim(\delta \mathbf{x})$ is the dimension of the state space, and the subscript i represents the i th column of the matrix.

2) Computation of Sigma Points ($\mathcal{X}_{i,k}$):

$$\begin{aligned}\mathcal{X}_{0,k} &= \delta \hat{\mathbf{x}}_k^+ \\ \mathcal{X}_{i,k} &= \delta \hat{\mathbf{x}}_k^+ + \left(\sqrt{n+\lambda}\right)\sqrt{\mathbf{P}_{k,i}^+}; \quad i = 1, 2, \dots, n \\ \mathcal{X}_{i+n,k} &= \delta \hat{\mathbf{x}}_k^+ - \left(\sqrt{n+\lambda}\right)\sqrt{\mathbf{P}_{k,i}^+}; \quad i = 1, 2, \dots, n\end{aligned}\quad (17)$$

where λ is a scaling parameter ($\lambda = -5$), which follows the $\lambda + n = 3$ rule, and $\sqrt{\mathbf{P}_{k,i}^+}$ is the Cholesky factor of \mathbf{P}_k

3) Prediction/Propagation of Sigma Points:

$$\mathcal{X}_{i,k+1} = f(\mathcal{X}_{i,k}); \quad i = 0, 1, \dots, 2n \quad (18)$$

where $f(\cdot)$ is a nonlinear state mapping function. Since f is linear, Φ is used instead of f in (18).

4) Unscented Transformation of State ($\delta \hat{\mathbf{x}}_{k+1}^-$) and Covariance (\mathbf{P}_{k+1}^-):

$$\begin{aligned}\delta \hat{\mathbf{x}}_{k+1}^- &= \sum_{i=0}^{2n} \mathbf{W}_i \mathcal{X}_{i,k+1} \\ \mathbf{P}_{k+1}^- &= \left(\sum_{i=0}^{2n} \mathbf{W}_i (\mathcal{X}_{i,k+1} - \delta \hat{\mathbf{x}}_{k+1}^-) (\mathcal{X}_{i,k+1} - \delta \hat{\mathbf{x}}_{k+1}^-)^T \right) + \mathbf{Q}.\end{aligned}\quad (19)$$

5) Updating Sigma Points:

$$\begin{aligned}\mathcal{X}_{0,k+1} &= \delta \hat{\mathbf{x}}_{k+1}^- \\ \mathcal{X}_{i,k+1} &= \delta \hat{\mathbf{x}}_{k+1}^- + \left(\sqrt{n+\lambda}\right)\sqrt{\mathbf{P}_{k+1,i}^-}; \quad i = 1, 2, \dots, n \\ \mathcal{X}_{i+n,k+1} &= \delta \hat{\mathbf{x}}_{k+1}^- - \left(\sqrt{n+\lambda}\right)\sqrt{\mathbf{P}_{k+1,i}^-}; \quad i = 1, 2, \dots, n.\end{aligned}\quad (20)$$

6) Unscented Transformation of Measurements ($\bar{\mathbf{z}}_{k+1}$):

$$\begin{aligned}\mathcal{Z}_{i,k+1} &= h(\mathcal{X}_{i,k+1}); \quad i = 0, 1, \dots, 2n \\ \bar{\mathbf{z}}_{k+1} &= \sum_{i=0}^{2n} \mathbf{W}_i \mathcal{Z}_{i,k+1}\end{aligned}\quad (21)$$

where $h(\cdot)$ is a nonlinear measurement mapping function.

7) Gain Computation:

$$\begin{aligned}\mathbf{P}_{k+1}^{\mathbf{z},\mathbf{z}} &= \left(\sum_{i=0}^{2n} \mathbf{W}_i (\mathcal{Z}_{i,k+1} - \bar{\mathbf{z}}_{k+1}) (\mathcal{Z}_{i,k+1} - \bar{\mathbf{z}}_{k+1})^T \right) + \mathbf{R} \\ \mathbf{P}_{k+1}^{\mathbf{x},\mathbf{z}} &= \left(\sum_{i=0}^{2n} \mathbf{W}_i (\mathcal{X}_{i,k+1} - \delta \hat{\mathbf{x}}_{k+1}^-) (\mathcal{Z}_{i,k+1} - \bar{\mathbf{z}}_{k+1})^T \right) \\ \mathbf{K}_{k+1} &= \mathbf{P}_{k+1}^{\mathbf{x},\mathbf{z}} (\mathbf{P}_{k+1}^{\mathbf{z},\mathbf{z}})^{-1}\end{aligned}\quad (22)$$

where $\mathbf{P}^{\mathbf{z},\mathbf{z}}$ is the covariance matrix in the transformed measurements with dimension M and $\mathbf{P}^{\mathbf{x},\mathbf{z}}$ is the cross-covariance matrix between the transformed states and the measurements with dimension $n \times M$.

8) Updated State ($\delta \hat{\mathbf{x}}_{k+1}^+$) and Covariance (\mathbf{P}_{k+1}^+):

$$\begin{aligned}\delta \hat{\mathbf{x}}_{k+1}^+ &= \delta \hat{\mathbf{x}}_{k+1}^- + \mathbf{K}_{k+1} (\mathbf{z}_{k+1} - \bar{\mathbf{z}}_{k+1}) \\ \mathbf{P}_{k+1}^+ &= \mathbf{P}_{k+1}^- - \mathbf{K}_{k+1} \mathbf{P}_{k+1}^{\mathbf{z},\mathbf{z}} \mathbf{K}_{k+1}^T.\end{aligned}\quad (23)$$



Fig. 2. Environment of first test case study (from Google Earth): signal blockage condition.

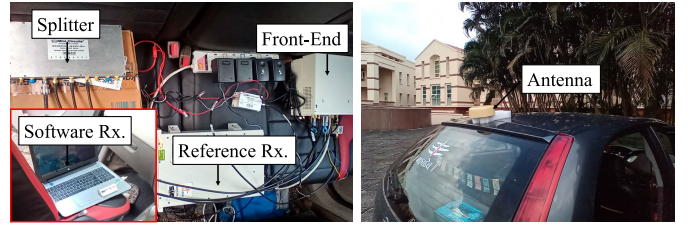


Fig. 3. Instrumental hardware setup for collecting NavIC measurements.

III. INSTRUMENTATION AND EXPERIMENTAL SETUP

A. Field Test Description

Two field tests were carried out to evaluate the performance of improved CA-DFVT NavIC receiver architecture in terms of its ability against signal blockage and interference conditions in urban canyon positioning. In the first test case, two separate second-generation universal software radio peripheral (USR2) devices synced together using a multiple-input and multiple-output (MIMO) cable were employed to collect the NavIC $L5$ - and S -band signals. The sampling was done at 10 MHz with intermediate frequency (IF) at 0 MHz. The RF front end was equipped in a car and the antenna was put on the car roof. The collected signals were stored in the laptop through 1-Gb Ethernet for postprocessing by the improved CA-DFVT receiver. The test case was carried out in a signal blockage situation within the university campus, where the car was driven through a basement.

The environment and instrumental hardware setup for the first test case are presented in Figs. 2 and 3, respectively. In this test, the car was moving at a constant speed of approximately 10 km/h. However, between the start point to endpoint, the car was stopped for a brief duration in the basement so that the visibility of satellites minimizes due to signal blockage. The total duration of the field test was approximately 165 s. A commercial multiconstellation (GPS L1/NavIC L5+S/SBAS L1) hardware receiver in its best configuration was used as the reference to calculate the positioning errors.

In the second test case, the same two USRP2 setups were used to collect the NavIC signals at 20- and 0-MHz sampling frequency and IF, respectively. For this test case, the antenna was intentionally exposed to signals from Wi-Fi, LTE, and Bluetooth devices. We employed a Wi-Fi D-Link DSL-2750U



Fig. 4. Environment and instrumental setup of second test case: interference in urban canyon from Wi-Fi, LTE, and Bluetooth signals.

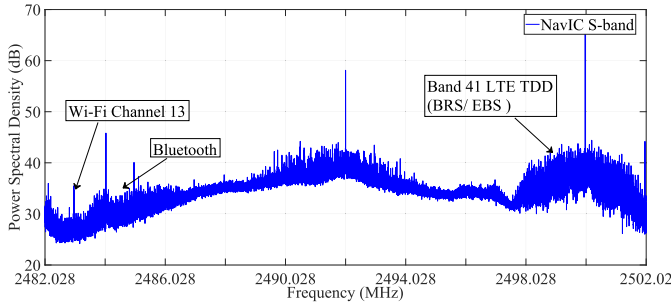


Fig. 5. Welch spectrum estimate of IF samples for NavIC S -band signal.

router, One-Plus mobile phone, and Bluetooth earpods to replicate the actual scenario of urban canyon, where signals from these open ISM band devices often interfere with the NavIC signal. Fig. 4 shows the environment of this case.

The signal strength of Wi-Fi, Bluetooth, and LTE was measured using a spectrum analyzer and was found to be -58 , -75 , and -64 dBm, respectively. During the signal recording, the mobile phone connected to the Bluetooth earpods was used to communicate with another person on the LTE network. Fig. 5 shows the frequency spectrum of the recorded NavIC S signal, where the interfering frequencies are highlighted. As mentioned earlier, these signals act as out-of-band interference for NavIC S -band signals; therefore, through this test experiment, the robustness of the improved CA-DFVT algorithm under interference conditions is evaluated.

IV. PERFORMANCE ASSESSMENT OF THE IMPROVED CA-DFVT NAVIC RECEIVER BASED ON MEASUREMENTS

In this section, the improved CA-DFVT receiver is tested against standalone $L5$, S -band VT, CA-DFVT-EKF, and CA-DFVT-UKF receiver architectures in the above two scenarios, to assess the performance of improved CA-DFVT. We present the analysis in three parts.

- 1) The positioning results in terms of 2-D horizontal errors and velocity estimation are presented. The positioning results are further supported by the analysis of estimated C/N_0 , I and Q correlations, pseudorange measurement residue, and pseudorange error measurements with and without Savitzky–Golay filtering before giving to the EKF navigation filter.

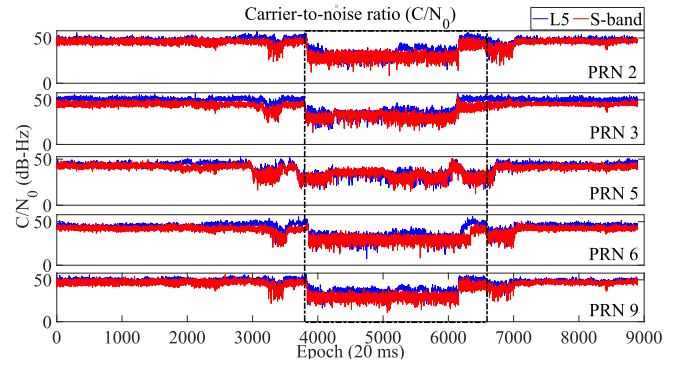


Fig. 6. C/N_0 values under blockage situation (test 1) for $L5$ and S -band.

- 2) The EKF navigation filter analysis is presented. This includes the analysis of the residue errors and convergence trend of the state vector elements over time. Finally, the σ -bounds of the state vectors are established.
- 3) The performance of all five receiver architectures, i.e., standalone $L5$, SVT, CA-DFVT-EKF, CA-DFVT-UKF, and improved CA-DFVT, was compared in terms of positioning accuracy. Except for CA-DFVT-UKF, the measurement residuals are analyzed for other architectures.

A. PVT Estimation Performance

1) *Test 1:* For the first test, the condition of signal blockage has been considered, as shown in Fig. 2. Because of the basement parking in this trajectory, the car encounters a small blockage area. While the car passed through the trajectory, it was briefly stationed in this basement. This resulted in reduced visibility of the satellites due to the obstruction for the stationary period. For this period, the antenna was unable to receive good signal strength, as shown by the estimated C/N_0 values of both NavIC $L5$ and S signals in Fig. 6.

In Fig. 6, significant fluctuations can be seen in all of the C/N_0 measurements. The degradation in C/N_0 measurements was approximately 15–16 dB-Hz for both NavIC $L5$ and S signals, which indicates that these signals are affected by blockage and clear LOS signals are not available. Signals from six satellites were tracked, but due to the unavailability of signal from NavIC PRN 4 after passing the blockage area, it was eliminated from the measurements and analysis.

The prompt I and Q correlation values from the scalar tracking are shown in Fig. 7, where a decrease in the correlation values can be observed. This decrease in correlation values indicates the adverse effect of signal blockage and weak signal reception. Due to this signal degradation, the estimation of positioning solutions is affected drastically, resulting in significant positioning errors. However, it is to be noted that for the blockage duration, the magnitude of correlation values does not go to an extreme zero value, which means that some amount of correlation was still present during the tracking process. For this reason, the chances of complete failure of the receiver's navigation processor are minimal, but the

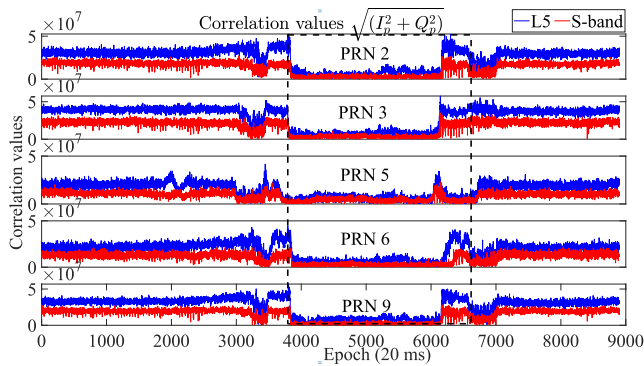


Fig. 7. Correlation values under blockage (test 1) for NAVIC $L5$ and S signals.

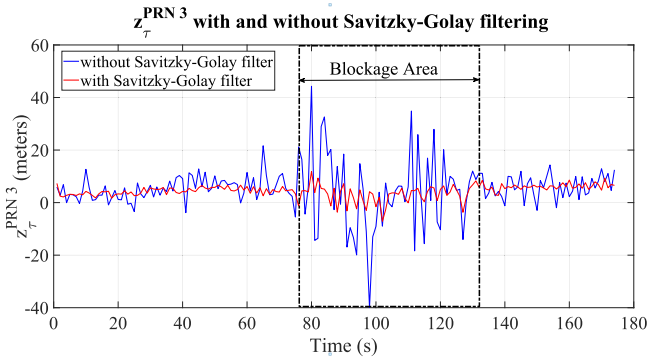


Fig. 8. Pseudorange error measurement values with and without Savitzky–Golay filtering for PRN 3 under the signal blockage test scenario.

overall performance of the receiver deteriorated and resulted in erroneous navigation solutions.

As in the proposed improved CA-DFVT, the estimated measurements are prefiltered using Savitzky–Golay before giving it to the EKF navigation filter. Therefore, to highlight its significance, an analysis of pseudorange error measurements before and after Savitzky–Golay filtering was carried out, and the results for the same are presented in Fig. 8. Since the discriminator outputs are pseudorange errors, these measurements should be zero. However, the measurements are not zero due to the noise caused by signal blockage, as seen in the blue trend. It is reasonable to consider the measurements outside a threshold as noise-corrupted outliers. The prefiltering process removes these outliers so that the noise in the measurements passed to the EKF is reduced. The clear effect of this filtering can be seen in Fig. 8, wherein, after Savitzky–Golay filtering, the outliers in pseudorange error measurement significantly got reduced.

Fig. 9 shows the pseudorange measurement residue also known as the innovation sequence in the EKF algorithm. The residue for CA-DFVT-UKF involves the transformation of states and measurements. Although the residues and its trend may be close for both EKF and UKF, the physical meaning may not be the same, hence not shown in Fig. 9. Moreover, the focus of this residual analysis is only to validate the stability of the proposed measurement model. It is important to note that Fig. 8 represents the measurement z_τ , whereas Fig. 9 represents $(z_\tau - \mathbf{H}\delta\hat{\mathbf{x}}^-)$; thus, both are

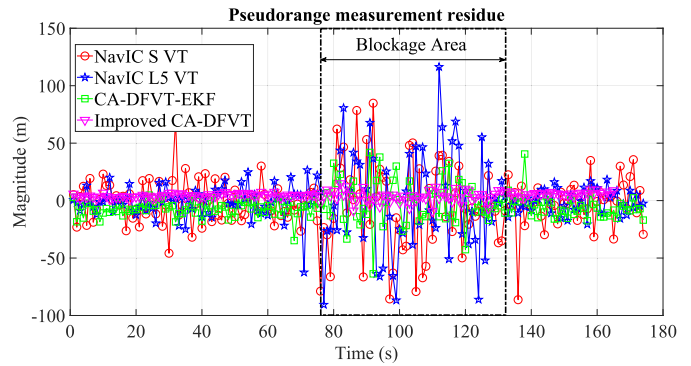


Fig. 9. Pseudorange measurement residue of PRN 3 under signal blockage condition (test 1).

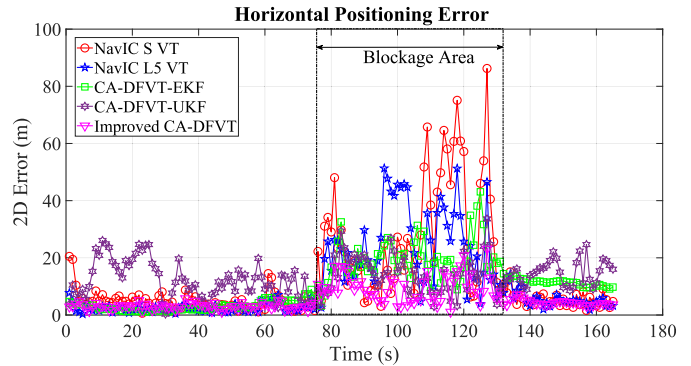


Fig. 10. 2-D positioning error for single-frequency VT, CA-DFVT-EKF, CA-DFVT-UKF, and improved CA-DFVT during dynamic test case 1 (signal blockage).

different quantities. z_τ is before it is fed to the EKF algorithm, and $(z_\tau - \mathbf{H}\delta\hat{\mathbf{x}}^-)$ is calculated as part of the EKF algorithm.

In Fig. 9, it is observed that the magnitude of pseudorange measurement residue of the improved CA-DFVT is very small compared to standalone $L5/S$ VT and CA-DFVT-EKF. The standard deviation (SD) for single-frequency S , $L5$, and CA-DFVT-EKF is 27.62, 25.59, and 22.62 m, respectively, whereas for the improved CA-DFVT, it is 3.47 m. This clearly indicates that the measurement errors in improved CA-DFVT are less compared to earlier methods. Moreover, for the blockage period, the measurements are smooth and consistent. As a result, under signal blockage conditions, it is able to deliver precise and accurate positioning solutions.

To evaluate the performance of the improved receiver architecture in more detail, we divided the complete trajectory into three segments as segments 1 (1–75 s), 2 (76–132 s), and 3 (133–174 s). The estimated states are in Earth-centered Earth-fixed (ECEF) frame. To calculate the horizontal position error, we transform the positioning results from ECEF into an east, north, and up (ENU) frame. The positioning error of all five receiver architectures during the test is shown in Fig. 10. Although the tracking results were estimated at every 20-ms epoch, the position computation by the improved CA-DFVT is carried out every 1 s. This is due to the filtering approach applied at the measurement model, in which every 999 samples are fit using the low-order polynomial. Therefore, for the sake

TABLE I
STATISTICS OF POSITIONING ERROR FOR TEST 1: SIGNAL BLOCKAGE CONDITION

Methods ↓ Statistics →	Segment 1 (1 – 75 s)			Segment 2 (76 – 132 s)			Segment 3 (133 – 174 s)		
	Max (m)	Mean (m)	SD (m)	Max (m)	Mean (m)	SD (m)	Max (m)	Mean (m)	SD (m)
NavIC S VT	20.502	5.001	3.562	86.238	28.353	20.457	15.091	5.382	2.650
NavIC L5 VT	7.751	2.447	1.519	51.312	24.270	13.762	14.153	5.464	2.805
CA-DFVT-EKF	8.924	3.107	1.741	43.088	19.392	7.548	13.711	11.342	1.221
CA-DFVT-UKF	26.066	12.190	6.499	33.617	14.358	6.849	24.643	14.939	4.232
Improved CA-DFVT	5.775	3.175	1.618	23.129	9.290	4.899	7.155	4.374	1.014

of comparison, all other approaches are scaled down to 1-s resolution. In fact, the reference receiver is used for ground truth output navigation solution at a 1-Hz rate only.

The positioning performances of single-frequency *L5/S*, CA-DFVT-EKF, CA-DFVT-UKF, and improved CA-DFVT are summarized in Table I. The 2-D rms position error for CA-DFVT-EKF is 1.0585 m. The error decreases to 0.5433 m for the improved CA-DFVT. In addition, the performance statistics, such as maximum, mean, and SD of the 2-D position error, indicate that the improved CA-DFVT performs better compared to single-frequency *L5/S* VT, CA-DFVT-EKF, and CA-DFVT-UKF. During the blockage period, 19.392 m of 2-D mean error is obtained for CA-DFVT-EKF with an SD of 7.548 m. The error decreases to 9.290 m for improved CA-DFVT. Surprisingly, the positioning error for CA-DFVT-UKF is relatively poor in all three segments, majorly for segment 3 when the car came out of the blockage area. However, for segment 2, the positioning error of CA-DFVT-EKF and UKF is closely related.

Based on the above analysis and statistics presented in Table I, it is evident that the proposed improved version of CA-DFVT receiver architecture outperforms the single-frequency VT and CA-DFVT-EKF/UKF approaches. During the blockage period, the improved CA-DFVT consistently provided navigation solutions with the least errors. Moreover, results also indicate that the standalone NavIC *S* signal in VT cannot provide precise and accurate positioning. This is possibly because of the interference and low signal strength of the NavIC *S* signal. In fact, in the case of the different versions of CA-DFVT, despite the fact that they employ two different frequencies, as the results show, their performance may get affected when the severe signal interruption occurs. In such cases, the improved CA-DFVT approach with its smoothing filtering by Savitzky–Golay on measurements helps offset the effects of external noises. This can be clearly observed in Fig. 10, where the degradation in positioning results obtained from improved CA-DFVT is less pronounced when compared to a standalone NavIC *L5/S* VT, specifically for the blockage period.

Fig. 11 shows the estimated velocity by the single-frequency *L5/S* VT, CA-DFVT-EKF/UKF, and improved CA-DFVT. In Fig. 11, the blockage part during the trajectory is highlighted, in which for the sake of clarity and better representation, we show a small portion of the total trajectory (especially blockage period). Ideally, during this blockage period, the velocity should be zero as the car was briefly stationed in

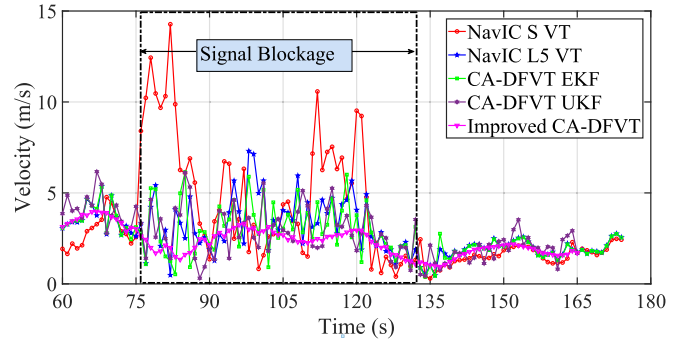


Fig. 11. Estimated velocity by different VT-based receiver architectures.

this area. However, it is observed that the *S*-band has larger fluctuations, while the variations in *L5*, CA-DFVT-EKF, and CA-DFVT-UKF are comparatively less. However, variations in estimated velocities in improved CA-DFVT are far smoother and consistent with respect to actual velocity errors.

Since the LOS signals are not available at this point, therefore, these estimations are based on the previous measurements by EKF/UKF navigation filter. However, compared to the single-frequency *L5/S* VT, the CA-DFVT-EKF/UKF shows considerably less fluctuation in the velocity estimation. On the other hand, the improved CA-DFVT shows even less fluctuations. Once the car comes out of the basement or blockage area, it immediately reacquires the signals, and estimates the velocity accurately. From the above analysis, it is noteworthy that even the performance of CA-DFVT-based on EKF/UKF gets degraded during severe blockage. However, this performance degradation is reduced in improved CA-DFVT. Subsequently, through different measurement analyses, it is shown that the degradation is less compared to the conventional single-frequency *L5/S* VT receiver architectures. The improved CA-DFVT recovers fast and gives accurate results once satellite signals are available.

2) *Test 2:* For the second test, the interference from Wi-Fi, Bluetooth, and LTE signals has been considered. The GNSS receiving antenna was exposed to these unlicensed *S*-band signals. Motivation of conducting this test was to explore the ability of improved CA-DFVT to track NavIC signals in the presence of these signals and to evaluate how accurate position solutions can be obtained. In this test, for first 48–55 s, the front end was allowed to record live signals without any interruptions. Later, the Wi-Fi router set to channel 13 was switched on, and Bluetooth-enabled mobile phone and earpods

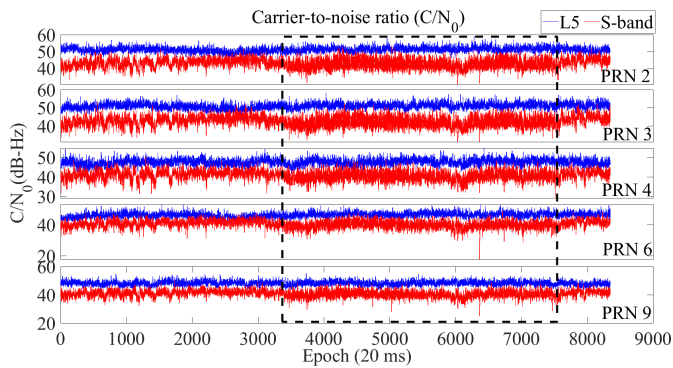


Fig. 12. C/N_0 values under interference condition (test 2) for $L5$ - and S -bands.

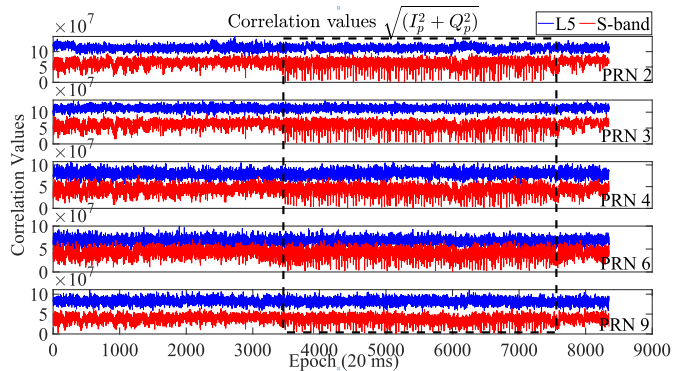


Fig. 13. In-phase prompt correlation values under interference condition (test 2) for $L5$ - and S -bands.

were engaged in making a phone call to another person on the LTE network.

Fig. 12 shows the estimated C/N_0 values of both NavIC $L5$ and S signals for this test. A drop in the C/N_0 measurements of NavIC S signal can be observed during the transmission phase of external signals. The C/N_0 measurements of PRNs 2–4 shows the maximum drop. The degradation in C/N_0 measurements was approximately 10–12 dB-Hz. A similar observation of degradation in the C/N_0 measurements of NavIC S signal was reported in [3], where the maximum drop was observed due to Wi-Fi channel 13.

Fig. 13 shows the prompt I and Q correlation values of scalar tracking for both NavIC $L5$ and S signals. Several inverted spikes can be observed in the correlation values of S signal for all PRNs, due to the interference in the received signals. However, the magnitude of these spikes is not the same for all PRNs. As observed from Fig. 13, PRNs 2–4 are the most severely affected by the interference.

A similar analysis as shown in Fig. 8 was carried out for the second test, i.e., with and without the Savitzky–Golay filtering under interference condition. It can be observed in Fig. 14 that the random fluctuations caused due to interference in the actual integrated measurements are removed by the Savitzky–Golay filter. These improved measurements when given to the navigation filter of the improved CA-DFVT result in better position estimates. To support this, the pseudorange measurement residue for single-frequency $L5/S$ VT, CA-DFVT-EKF, and improved CA-DFVT are shown in Fig. 15. As discussed

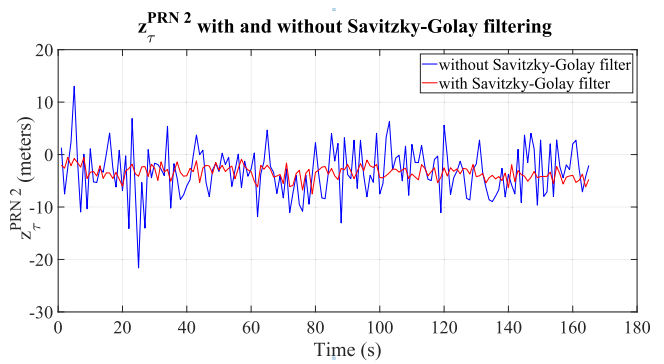


Fig. 14. Pseudorange error measurement values with and without Savitzky–Golay filtering for PRN 2 under the signal interference test scenario.

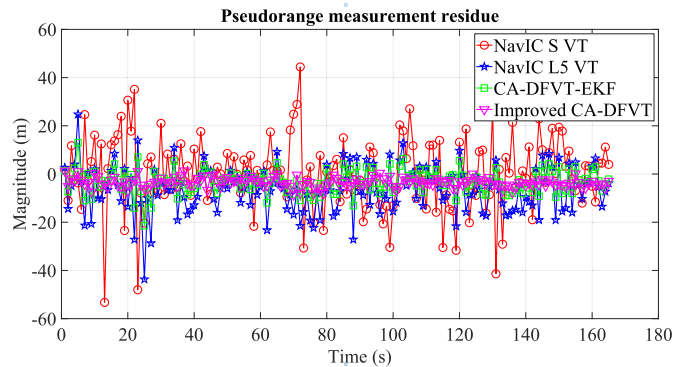


Fig. 15. Pseudorange measurement residue of PRN 2 under the interference condition.

earlier, the pseudorange residue for CA-DFVT-UKF is not shown here because of the transformation of states and measurements done in CA-DFVT-UKF.

As can be observed in Fig. 15, the pseudorange measurement residue of NavIC S VT shows several spikes throughout the test. These spikes intensified during the latter part of the signal. As expected, this is due to the interference from Wi-Fi, Bluetooth, and LTE signals triggered during the latter part of the signal recording. Ideally, the pseudorange measurement residue error must be zero; however, variations in signal and several error sources cause some magnitude. Among the three VT approaches, improved CA-DFVT shows the least pseudorange measurement error, which eventually means that the improved CA-DFVT can provide better positioning results using the improved dual-frequency measurements. Moreover, due to the bidirectional filtering and additional measurement smoothing, the estimates measurements are smoother compared to other approaches. This also proves the effectiveness of the proposed receiver architecture under interference conditions.

The 2-D horizontal positioning errors are calculated with reference to the ground truth for single-frequency $L5/S$, CADFVT-EKF, CA-DFVT-UKF, and improved CA-DFVT, as shown in Fig. 16. As can be observed in Fig. 16, the single-frequency S VT has a higher positioning error compared to that of the other four approaches. The 2-D rms position error for CADFVT-EKF is 0.3077 m. The error decreases to 0.1475 m for the improved CA-DFVT. The positioning

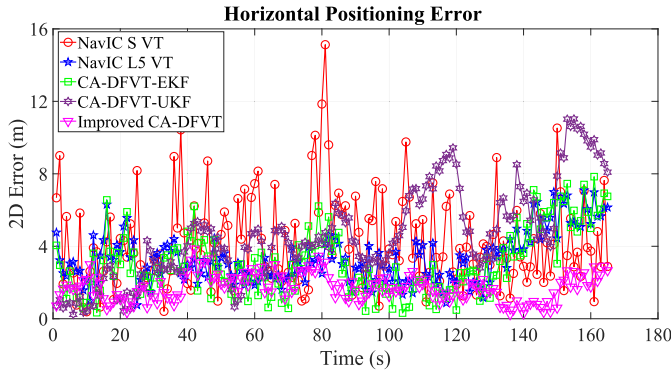


Fig. 16. Positioning error of stationary test case 2 (interference).

 TABLE II
 STATISTICS OF POSITIONING ERROR FOR TEST 2:
 INTERFERENCE CONDITION

Methods ↓ Statistics →	Max (m)	Mean (m)	SD (m)
NavIC S VT	15.128	4.224	2.546
NavIC L5 VT	7.094	3.353	2.217
CA-DFVT-EKF	7.842	3.041	1.815
CA-DFVT-UKF	11.029	4.616	2.599
Improved CA-DFVT	3.859	1.731	0.743

performances in terms of maximum, mean, and SD of these VT approaches are summarized in Table II. A maximum 2-D mean error of 4.616 m with an SD of 2.599 m is observed in CA-DFVT-UKF, whereas the least is observed in the case of the improved CA-DFVT. Moreover, the performance statistics for single-frequency L5 VT and CA-DFVT-EKF are at a very close margin.

B. Analysis of Residual Errors

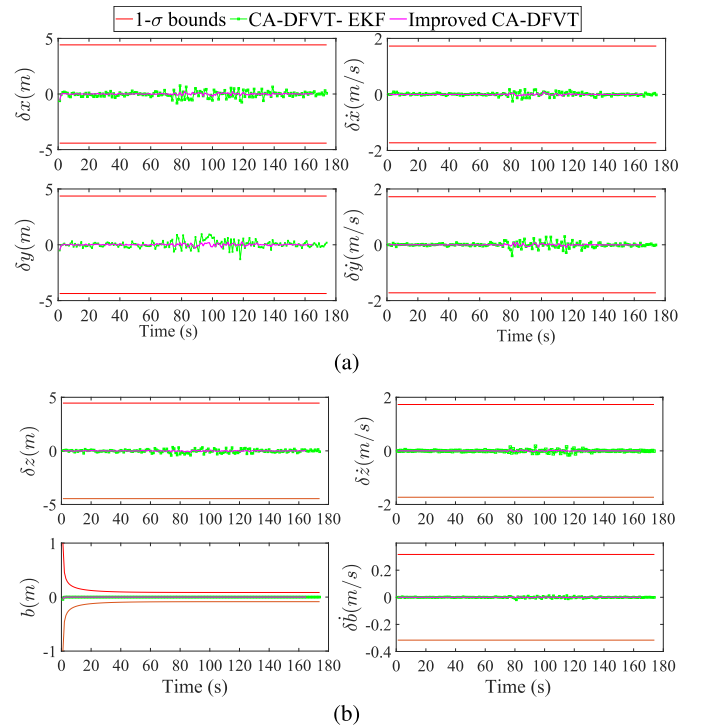
The EKF attempts to reduce the error in the estimated states over time. As CA-DFVT-EKF and improved CA-DFVT use a modified measurement model in the EKF navigation filter. Therefore, it is necessary to verify whether the new measurement model of both CA-DFVT-EKF and improved CA-DFVT does not cause any instability in the performance of the EKF navigation filter. Since the states consist of the error in the position and velocity, the trend of the elements of the states $\delta \mathbf{x}$ is a direct measure of how effectively the EKF is able to predict the true states of the receiver. For the stability analysis, a residual error analysis is carried out. A residue error indicates how effectively the measurement updates the state vector.

The residual error vector \mathbf{e}_k for the states $\delta \mathbf{x}$ and its 1σ -bound at each epoch k is computed as [21]

$$\begin{cases} \mathbf{e}_k = \mathbf{K}_k(\mathbf{z}_k - \mathbf{h}_k(\delta \mathbf{x}_k)) \\ \sigma_k^2 = \text{diag}((\mathbf{I} - \mathbf{K}_k \mathbf{H}_k) \mathbf{P}_k^-) \end{cases} \quad (24)$$

where $\mathbf{h}_k(\delta \mathbf{x}_k)$ is the observation function that relates the predicted states vector $\delta \mathbf{x}_k$ with the observations.

Fig. 17 shows the trend in the states and σ bounds at each epoch k for test 1 (signal blockage). The σ -bounds are obtained by taking the square root of the computed variance.


 Fig. 17. (a) and (b) Residual error of test 1 (blockage scenario): the state vector elements $\mathbf{x}(i)$, $i = 1, 2, \dots, 8$, and the corresponding 1σ bounds.

Here, we presented the 1σ -bounds, and it is observed that they are within the bounds, which also means that they will also satisfy the conventional 3σ . Typically, the EKF achieves a steady state after a couple of iterations. Thus, the residue values shown in Fig. 17 are the values after achieving the steady state.

As can be observed in Fig. 17, the residual errors are $\pm 1\sigma$ confidence interval for the states. The states b and δb converge in a very short time, while the other states also converge within a small confidence interval. Even for the duration of signal blockage, the residual errors are within this small confidence interval for both VT approaches. A similar phenomenon was observed for the interference condition and hence not shown here. Since all the states are well within the σ -bounds, this confirms the robustness and consistent performance of both CA-DFVT-EKF and improved CA-DFVT approaches. Although, for both approaches, the residue errors are within the sigma bounds, however, the residue errors for improved CA-DFVT have less noise variance compared to CA-DFVT-EKF. The above analysis shows that the measurement model of the improved CA-DFVT is stable and can perform well under short signal blockage and interference conditions in urban positioning environments.

V. CONCLUSION

In this article, we presented a modified version of CA-DFVT receiver architecture based on bidirectional filtering through RTS and measurement smoothing using the Savitzky–Golay filter. We illustrated how the performance of CA-DFVT-EKF can be improved in signal-constraint environments, such as those with signal blockage and interference.

A detailed performance evaluation of various VT approaches for NavIC signals in terms of positioning and EKF analysis was presented. In addition, UKF-based CA-DFVT was presented, in which the positioning results of the improved CA-DFVT were compared to single-frequency $L5/S$ VT, original CA-DFVT-EKF, and CA-DFVT-UKF approaches. It was observed that the UKF-based CA-DFVT does not perform well most of the times compared to other approaches. The presented positioning results qualitatively and quantitatively validate the effectiveness of improved CA-DFVT in harsh urban environments. Moreover, the EKF residual analysis proves the stability of the EKF measurement model in the improved CA-DFVT. It shows fewer errors in the state vector elements over time when compared to the conventional single-frequency $L5/S$ VT measurement model. Hence, the improved CA-DFVT is an effective approach capable of producing robust and accurate positioning results in signal-constraint environments. This work also suggests that the proposed improved CA-DFVT architecture could be a potential approach that other GNSS systems can adopt. In future work, we intend to extend the work to a more advanced tracking algorithm such as α - β filter as an estimation approach instead of traditional Kalman filtering.

REFERENCES

- [1] V. G. Rao, G. Lachapelle, and S. B. VijayKumar, "Analysis of IRNSS over Indian subcontinent," in *Proc. Int. Tech. Meeting Inst. Navigat.*, 2011, pp. 1150–1162.
- [2] A. Dey, L. M. Joshi, R. Chhibba, and N. Sharma, "A study of ionospheric effects on IRNSS/NavIC positioning at equatorial latitudes," *Adv. Space Res.*, vol. 68, no. 12, pp. 4872–4883, Dec. 2021.
- [3] A. Dey, K. Iyer, and N. Sharma, "S-band interference detection and mitigation using a vector tracking-based NavIC software receiver," in *Proc. 34th Int. Tech. Meeting Satell. Division Inst. Navigat. (ION GNSS)*, St. Louis, MO, USA, Sep. 2021, pp. 3464–3476.
- [4] F. Dovis, *GNSS Interference Threats and Countermeasures*. Norwood, MA, USA: Artech House, 2015.
- [5] E. M. Copps, G. J. Geier, W. C. Fidler, and P. A. Grundy, "Optimal processing of GPS signals," *Navigation*, vol. 27, no. 3, pp. 171–182, Sep. 1980.
- [6] J. J. Spilker Jr., *Fundamentals of Signal Tracking Theory*. Washington, DC, USA: Amer. Inst. Aeronaut. Astronaut., 1995, pp. 245–327.
- [7] S. Zhao and D. Akos, "An open source GPS/GNSS vector tracking loop-implementation, filter tuning, and results," in *Proc. Int. Tech. Meeting Inst. Navigat.*, 2011, pp. 1293–1305.
- [8] F. M. G. Sousa and F. D. Nunes, "Performance analysis of a VDFLL GNSS receiver architecture under ionospheric scintillation and multipath conditions," in *Proc. IEEE/ION Position, Location Navigat. Symp.*, May 2014, pp. 602–611.
- [9] H. Y. F. Elghamrawy, M. Tamazin, and A. Noureldin, "Investigating the benefits of vector-based GNSS receivers for autonomous vehicles under challenging navigation environments," *Signals*, vol. 1, no. 2, pp. 121–137, Oct. 2020.
- [10] A. Dey and N. Sharma, "Investigating the performance benefits of vectorized NavIC receiver over federated NavIC receiver in semi-urban environments," in *Proc. URSI Regional Conf. Radio Sci. (URSI-RCRS)*, Dec. 2022, pp. 1–4.
- [11] M. Lashley, D. M. Bevely, and J. Y. Hung, "Performance analysis of vector tracking algorithms for weak GPS signals in high dynamics," *IEEE J. Sel. Topics Signal Process.*, vol. 3, no. 4, pp. 661–673, Aug. 2009.
- [12] B. Xu, Q. Jia, and L.-T. Hsu, "Vector tracking loop-based GNSS NLOS detection and correction: Algorithm design and performance analysis," *IEEE Trans. Instrum. Meas.*, vol. 69, no. 7, pp. 4604–4619, Jul. 2020.
- [13] T. Pany and B. Eissfeller, "Use of a vector delay lock loop receiver for GNSS signal power analysis in bad signal conditions," in *Proc. IEEE/ION Position, Location, Navigat. Symp.*, Apr. 2006, pp. 893–903.
- [14] S. Zhao, M. Lu, and Z. Feng, "Implementation and performance assessment of a vector tracking method based on a software GPS receiver," *J. Navigat.*, vol. 64, no. S1, pp. S151–S161, Nov. 2011.
- [15] A. Tabatabaei, M. R. Mosavi, H. S. Shahhoseini, and K. Borre, "Vectorized and federated software receivers combining GLONASS and GPS," *GPS Solutions*, vol. 21, no. 3, pp. 1331–1339, Jul. 2017.
- [16] A. Tabatabaei and M.-R. Mosavi, "Performance analysis of GLONASS integration with GPS vectorised receiver in urban canyon positioning," *Surv. Rev.*, vol. 51, no. 368, pp. 460–471, Sep. 2019.
- [17] E. Shytermeja, A. Garcia-Pena, and O. Julien, "Performance comparison of a proposed vector tracking architecture versus the scalar configuration for a L1/E1 GPS/Galileo receiver," 2019, *arXiv:1905.11022*.
- [18] X. Chen, X. Wang, and Y. Xu, "Performance enhancement for a GPS vector-tracking loop utilizing an adaptive iterated extended Kalman filter," *Sensors*, vol. 14, no. 12, pp. 23630–23649, Dec. 2014.
- [19] M. G. Petovello and G. Lachapelle, "Comparison of vector-based software receiver implementations with application to ultra-tight GPS/INS integration," in *Proc. 19th Int. Tech. Meeting Satell. Division Inst. Navigat.*, 2006, pp. 1790–1799.
- [20] J. Wendel, J. Metzger, R. Moenikes, A. Maier, and G. F. Trommer, "A performance comparison of tightly coupled GPS/INS navigation systems based on extended and sigma point Kalman filters," in *Proc. 18th Int. Tech. Meeting Satell. Division Inst. Navigat.*, 2005, pp. 456–466.
- [21] X. Tang, G. Falco, E. Falletti, and L. Lo Presti, "Practical implementation and performance assessment of an extended Kalman filter-based signal tracking loop," in *Proc. Int. Conf. Localization GNSS (ICL-GNSS)*, Jun. 2013, pp. 1–6.
- [22] A. Dey, K. Iyer, B. Xu, N. Sharma, and L.-T. Hsu, "Carrier-aided dual-frequency vectorized tracking architecture for NavIC signals," *IEEE Trans. Instrum. Meas.*, vol. 71, pp. 1–13, 2022.
- [23] X. Mao, M. Wada, and H. Hashimoto, "Investigation on nonlinear filtering algorithms for GPS," in *Proc. Intell. Vehicle Symp.*, Mar. 2002, pp. 64–70.
- [24] K.-H. Kim, J.-H. Song, and G.-I. Jee, "The GPS vector tracking loop based on the iterated unscented Kalman filter under the large initial error," in *Proc. Eur. Control Conf. (ECC)*, Aug. 2009, pp. 3701–3706.
- [25] Z. Sun, X. Wang, S. Feng, H. Che, and J. Zhang, "Design of an adaptive GPS vector tracking loop with the detection and isolation of contaminated channels," *GPS Solutions*, vol. 21, no. 2, pp. 701–713, Apr. 2017.
- [26] A. Savitzky and M. J. E. Golay, "Smoothing and differentiation of data by simplified least squares procedures," *Anal. Chem.*, vol. 36, no. 8, pp. 1627–1639, Jul. 1964.
- [27] H. E. Rauch, F. Tung, and C. T. Striebel, "Maximum likelihood estimates of linear dynamic systems," *AIAA J.*, vol. 3, no. 8, pp. 1445–1450, Aug. 1965.
- [28] Z. Gao, M. Ge, Y. Li, W. Shen, H. Zhang, and H. Schuh, "Railway irregularity measuring using Rauch–Tung–Striebel smoothed multi-sensors fusion system: Quad-GNSS PPP, IMU, odometer, and track gauge," *GPS Solutions*, vol. 22, no. 2, pp. 1–14, Apr. 2018.
- [29] S. S. Haykin and S. S. Haykin, *Kalman Filtering and Neural Networks*. Hoboken, NJ, USA: Wiley, 2001.
- [30] K. Ito and K. Xiong, "Gaussian filters for nonlinear filtering problems," *IEEE Trans. Autom. Control*, vol. 45, no. 5, pp. 910–927, May 2000.
- [31] P. C. P. M. Pardal, H. K. Kuga, and R. V. De Moraes, "Analyzing the unscented Kalman filter robustness for orbit determination through global positioning system signals," *J. Aerosp. Technol. Manage.*, vol. 5, no. 4, pp. 395–408, Nov. 2013.



Abhijit Dey (Member, IEEE) received the B.E. degree from the Department of Electronics and Communication Engineering, North Maharashtra University, Jalgaon, MH, India, in 2011, and the master's degree in radio frequency and microwave engineering in 2014. He is currently pursuing the Ph.D. degree with the Department of Electrical and Electronics Engineering, Birla Institute of Technology and Science Pilani, K K Birla Goa Campus, Sancoale, Goa, India.

He was a Junior Research Fellow in the ISRO-funded project with the Department of Electrical and Electronics Engineering, Birla Institute of Technology and Science at Pilani, from 2017 to 2019. He was a Visiting Ph.D. Researcher with the Department of Aeronautical and Aviation Engineering, The Hong Kong Polytechnic University, Hong Kong, SAR, China, from April to October 2021. His research interests include signal processing in software-defined global navigation satellite system (GNSS) receivers, interference, and ionospheric scintillation detection and mitigation techniques for GNSS systems.



Kaushik Iyer received the B.E. degree from the Department of Electrical and Electronics Engineering, Birla Institute of Technology and Science at Pilani, Pilani, India, in 2021. He is currently pursuing the M.Sc. degree in robotics and autonomous systems with the Department of Electrical Engineering, Arizona State University, Tempe, AZ, USA.

He was a Research Assistant with the Space Systems Laboratory (SSL), Indraprastha Institute of Information Technology (IIIT-Delhi), New Delhi, India, from June to December 2021. His research

interests include nonlinear control theory, adaptive signal processing, and Bayesian estimation with applications in space navigation, autonomous systems, and robotics.



Nitin Sharma received the Ph.D. degree from the Birla Institute of Technology and Science Pilani, Pilani, India, in 2014.

He is currently an Associate Professor with the Department of Electrical and Electronics Engineering, Birla Institute of Technology and Science Pilani. His current research interests include optimization in wireless communication, resource allocation and management for wireless and wired communications, cognitive radio, green communication technologies, machine to machine (M2M)/the Internet of Things (IoT) communications, cloud communication, and evolutionary computations. He is also working in the area of global navigation satellite system (GNSS) signal processing.



Bing Xu (Member, IEEE) received the B.E. and Ph.D. degrees in network engineering and navigation guidance and control from the Nanjing University of Science and Technology, Nanjing, China, in 2012 and 2018, respectively.

He was a Post-Doctoral Fellow with the Department of Aeronautical and Aviation Engineering, The Hong Kong Polytechnic University, Hong Kong, SAR, China, from August 2018 to April 2020, where he is currently a Research Assistant Professor. His current research interests include signal processing

in software-defined global navigation satellite system receivers.



Li-Ta Hsu (Senior Member, IEEE) received the B.S. and Ph.D. degrees in aeronautics and astronautics from National Cheng Kung University, Tainan, Taiwan, in 2007 and 2013, respectively.

He was a Post-Doctoral Researcher with the Institute of Industrial Science, The University of Tokyo, Tokyo, Japan. In 2012, he was a Visiting Scholar with the Faculty of Engineering, University College London, London, U.K. He is currently an Associate Head and an Associate Professor with the Department of Aeronautical and Aviation Engineering, The

Hong Kong Polytechnic University, Hong Kong, SAR, China. His current research interests include global navigation satellite system positioning in challenging environments and localization for autonomous driving vehicles and unmanned aerial vehicles.

Dr. Hsu has been an Associate Fellow of the Royal Institute of Navigation (RIN) and a Council Member of the Institute of Navigation (ION) since 2019.